Impact of P3/P2 Mixed Phase on the Structural and Electrochemical Performance of $Na_{0.75}Mn_{0.75}Al_{0.25}O_2$ Cathode

Hari Narayanan Vasavan ^a, Manish Badole ^a, Samriddhi Saxena ^a, Velaga Srihari^b, Asish Kumar Das ^a, Pratiksha Gami ^a, Sonia Deswal ^c, Pradeep Kumar ^c, and Sunil Kumar ^{a,d,*}

^a Department of Metallurgical Engineering and Materials Science, Indian Institute of Technology Indore, Simrol, 453552, India.

^b High Pressure & Synchrotron Radiation Physics Division, Bhabha Atomic Research Centre, 400085 Mumbai, India

^c School of Physical Sciences, Indian Institute of Technology Mandi, Himachal Pradesh, 175005, India

^d Center for Electric Vehicle and Intelligent Transport Systems, Indian Institute of Technology Indore, Simrol, 453552, India.

* Corresponding Author: sunil@iiti.ac.in

Abstract

The biphasic nature is known to enhance the structural stability and electrochemical properties of layered oxide cathodes. Herein, we have synthesised Na_{0.75}Mn_{0.75}Al_{0.25}O₂ (NMA) with different P2/P3 phase fractions, tuned by modifying the calcination temperature. Rietveld refinement of XRD data showed a continuous reduction in the P3 phase fraction with increased calcination temperature. NMA sample calcined at 650 °C (NMA-650) with ~ 52% P3 and 48% P2 phases showed good rate performance and a high specific capacity of 150 mAh g⁻¹ at 0.1C with 80% capacity retention after 200 cycles between 1.5-4.2 V. The enhanced electrochemical performance is attributed to the material's morphology and improved structural durability. Interestingly, *operando* Synchrotron XRD data of NMA-650 and NMA-750 (sample calcined at 750 °C) showed a continued existence of the P3 phase in both compounds during charging-discharging in the 1.5-4.2 V range. Further, the P3 unit cell showed only a 0.5% increase in volume compared to 1.5% in NMA-750 during cycling. The enhanced electrochemical properties of NMA-650 are attributed to the synergistic effect of P3/P2 phase coexistence in the material.

KEYWORDS: Layered oxides; Biphasic cathode; *Operando* Synchrotron XRD Electrochemical behaviour; Rate performance

1. Introduction

The economic benefits of sodium-ion batteries (NIBs) have allowed them to emerge as a favourable candidate for replacing the ubiquitous Li-ion batteries (LIBs) in stationary storage applications and mid-to-low-range electric vehicles [1-5]. Along with the considerably higher abundance of sodium, NIBs have a nearly identical charge storage mechanism and components as LIBs, allowing them to be seamlessly integrated into the current battery manufacturing eco-systems [6-11]. Cathodes in NIBs are the primary source of Na ions and

play a significant role in determining most performance characteristics. Research activities into cathode materials for NIBs have been centered around 3 different types of cathode materials: Layered oxides (LOs), NASICON, and Prussian blue analogs. Even though NASICON-based cathodes have shown a relatively high cyclic performance and cathodes based on Prussian blue analogs have demonstrated capacities close to 150 mAh g⁻¹, layered oxide (LO) based cathodes (Na_xTMO₂) are generally considered to have the edge over the others in terms of rate performance and ease of synthesis [9, 12-14].

LOs are mainly categorized into P2-type, P3-type, and O3-type based on their thermodynamic stability. In the P2-type structure, Na-ions occupy 2 different prismatic sites, which are either face-sharing (Na_2) or edge-sharing (Na_1) with the transition metal octahedron (TM-O₆) [15]. The Na ion concentration in P2-type materials is typically less than 0.75, although Na ion concentration is also reported to be as high as 0.85 in some of the P2-type LOs [12, 16]). As per Pauling's rules, edge-sharing (Na_1) sites would contain more Na ions (edge-shared polyhedra provide better stability to the crystal than the face-shared due to the larger distance between Na⁺ and Mn^{3+/4+}). In P3-type materials, all prismatic sites are crystallographically equivalent Na sites, while Na ions in the O3-type compounds occupy octahedral sites [15].

The structural and electrochemical properties of P2 and O3-type compounds have been extensively explored in the literature [4, 17-20]. P2-type materials have lower activation energies for Na ions and hence show better rate and cyclic performance than O3-type compounds, which usually exhibit higher specific capacities [12, 21, 22]. In comparison, reports on P3-type materials mostly revolve around those obtained electrochemically during the charging of O3 cathodes [17, 23-26]. Only a handful of studies deal with the structural and electrochemical properties of thermodynamically prepared P3-type materials where high diffusion coefficients comparable to those of P2-type materials are reported [24, 26-29].

However, P3-type materials tend to undergo extensive structural changes during cycling, rendering these materials with inferior cyclability. This is because O3, O'3, and P'3 phases that form at lower and higher voltages do not support fast Na-ion kinetics, severely limiting the rate performance of P3-type materials [29-31].

Among different cathode materials identified for NIBs, compounds based on manganese are widely studied. In LOs, Mn ions are usually paired with other active and inactive ions, such as Ni, Cu, Al, Mg, etc., to improve their structural properties. In most research articles on Mn-based layered oxides, Mn is paired with another active ion, such as Ni, to decrease the concentration of Mn³⁺ [19, 30, 32-34]. Mn³⁺ ions are Jahn-Teller active and are known to cause irreversible phase transformations in layered oxides during cycling. Hence, in most cases, Mn ions are partially replaced with other ions with a 2+ oxidation state to keep the manganese oxidation to 4+ and are also cycled in the 2-4.2 V voltage range where Mn^{4+/3+} redox reactions do not materialise [13, 32, 35-38]. This effectively reduces Mn⁴⁺ ions to a supporting role, acting as only pillar ions, drastically reducing the materials' specific capacity [21, 39-41].

Herein, we report on a novel method to suppress the structural modifications brought about by the activation of Mn^{3+/4+} redox reactions by preparing a P3/P2 biphasic Na_{0.75}Mn_{0.75}Al_{0.25}O₂ (NMA) where 25% of the Mn ions were substituted with Al³⁺ ions. An inactive Al³⁺ was chosen to act as a pillar ion during the charge/discharge process. It has a similar ionic radius as Mn⁴⁺ in an octahedral configuration that prevents transition metal ordering. Along with introducing Al³⁺, a biphasic P2/P3 type cathode configuration was adopted to stabilise the cathode structure during cycling further. Compared to the widely reported P2/O3 biphasic cathode, the concentration of the P2 and P3 phases in the P2/P3 biphasic cathode was found to be dependent on the calcination temperature, allowing us to prepare the cathode with the desired phase concentration [14, 19, 25, 26, 35]. Moreover, the

lower calcination temperature required for P3-type materials was instrumental in obtaining the desired P2/P3 phase fractions at lower calcination temperatures. This was found to have profound implications on the morphology and electrochemical properties of the cathode material, with P3 dominant biphasic cathodes showing substantially superior rate performance and cyclic stability compared to monophasic P2 cathodes that formed at higher temperatures. Further, the manifestation of the synergetic effect between the two phases mitigated the effects of severe structural distortions induced during cycling, resulting in a better cyclability of the biphasic cathodes.

2. Experimental

2.1 Synthesis

A conventional sol-gel method was adopted in preparing the series of cathode materials. Stoichiometric amounts of Manganese (II) acetate tetrahydrate, aluminium nitrate nonahydrate, and sodium carbonate were dissolved in DI water and stirred for 6 h. Then, ethylene glycol and citric acid were added. The homogeneous solution was allowed to stir for another 12 h and was heated to produce a gel. The gel was then dried and subsequently ground to obtain a powder. The powder was heat treated at 550 °C in air for 12 h and calcination at different temperatures $(600 - 800 \, ^{\circ}\text{C})$ to obtain the final product.

2.2 Structural Characterization

The powder x-ray diffraction (XRD) patterns were obtained at room temperature using Malvern Pan Analytica's, Empyrean, diffractometer (Cu-Kα radiation source) between 10°-80° 2θ range and the crystallographic data was obtained after Rietveld refinement of the XRD data using *TOPAS Academic* (version 6) software package [42]. The bond-valence site energy (BVSE) calculation was performed using softBV software developed by Chen and

Adams [43]. The SEM images were obtained using a Joel field emission scanning electron microscope (model JEOL-7610) with energy-dispersive x-ray spectroscopy (EDS) for elemental mapping. X-ray photoelectron spectra (XPS) were obtained using a Thermofisher Scientific - Naxsa base with an Al Kα X-ray source (1486.6 eV). *Operando* Synchrotron XRD studies were carried out in transmission mode at the Extreme Conditions Angle Dispersive/Energy Dispersive Synchrotron X-ray diffraction (BL11) at Indus-2 beamline (RRCAT) with a beam wavelength of 0.7302 Å and beam energy of 2.5 GeV. *Operando* studies were performed on a CR2032 coin cell with 3 mm holes sealed using Kapton films in the cathode and anode casings.

2.3 Electrochemical Characterisation.

The cathode slurry was prepared by mixing the active material, Ketjen black, and PVDF binder in NMP in a wt. ratio of 75:10:15, which was coated on an Al foil current collector and dried. CR2032 coin cells were fabricated for electrochemical tests using a Na metal counter electrode, a Whatman GF/D filter paper separator, and 1M NaClO4 in Ethylene Carbonate - Propylene Carbonate (vol. ratio of 1:1) electrolyte. The cyclic voltammetry (CV) tests were performed at a scan rate of 0.1 mV/s using a Keithley Model 2450-EC Source Meter Unit. Galvanometric charge-discharge (GCD) tests and the galvanometric intermittent titration technique (GITT) were performed on a Neware battery tester (CT-4008T). The rate performance of the samples was evaluated between 0.1C – 4C rates, and the cyclic performance was monitored for 200 cycles at 1C between 1.5 V and 4.2 V. The mass loading for the samples was varied between 2-3 mg/cm², and C-rates were calculated assuming a nominal capacity of 150 mAh/g. Impedance measurements were performed using a computer-controlled LCR meter (model: ZM 2376, NF Corp.) equipped with an internal DC bias up to 5 V over a 1 Hz – 1 MHz frequency range at room temperature

2. Results and Discussion

3.1 Structural Characteristics

Various Na_{0.75}Mn_{0.75}Al_{0.25}O₂ samples were prepared by varying the calcination temperature between 600 °C and 800 °C. Figure 1(a) shows the room temperature XRD patterns of Na_{0.75}Mn_{0.75}Al_{0.25}O₂ (NMA-x: x denotes the calcination temperature in °C) samples calcinated at different temperatures along with the Bragg positions of P3 (JCPDS No. 04-020-1860) and P2 (JCPDS No.27-0751) type phases. The figure shows an unreacted phase at 600 °C and a P2/P3 mixed phase forming at around 650 °C with diffraction peaks corresponding to the P2 phase gradually increasing in intensity with increased calcination temperature. At a calcination temperature of 800 °C, a monophasic P2-type structure is obtained with no peaks corresponding to the P3 phase discernible in the XRD pattern. This is confirmed by the Rietveld refinement of the XRD data (Fig. 1(b)), which shows the P2:P3 phase ratio around ~ 52:48 for the sample calcined at 650 °C. The fraction of the P2 phase increased to ~ 72.5% in the sample calcined at 750 °C, and a pure P2-type material was obtained at 800 °C. The conversion of the P3 to P2 phase upon an increase in calcination temperature observed in this study is in line with other reports in the literature where the appearance of a P3 phase is often reported at lower calcination during the synthesis of P2type materials [17, 26]. This study demonstrates the control of the P3/P2 phase fraction in Na_{0.75}Mn_{0.75}Al_{0.25}O₂ with calcination conditions.

The crystallographic parameters of the NMA-x series of materials obtained after refinement are presented in Table 1. The refinement results show that the crystallographic volume for P2 and P3 type phases remained largely invariant, ~78.4 ų and ~117.4 ų, respectively, in all samples. The unit cell volume of P3 is about 1.5 times the P2 phase, which is expected as the number of formula unit cells in one crystallographic unit cell (Z) for P2 is 2, while for P3, Z is 3. The area of rectangular faces of the triangular prisms in P2 and P3 type structures, which

forms a major bottleneck to Na ion conduction, was around 11.11 Å². This points to similar inter-layer spacings (in both the TM-O and Na-O layers) in the P2 and P3 phases. Although P3 is often regarded as an ordered P2 phase where Na ions reside in a single crystallographically equivalent lattice site as opposed to the 2 different sites in the latter, the structural information obtained through Rietveld refinement for NMA-*x* series materials suggests similar Na⁺ conduction dynamics in both the phases. The detailed structural parameters of the P2 and P3 type NMA obtained from the Rietveld refinement of XRD patterns are given in Tables S1 and S2, respectively.

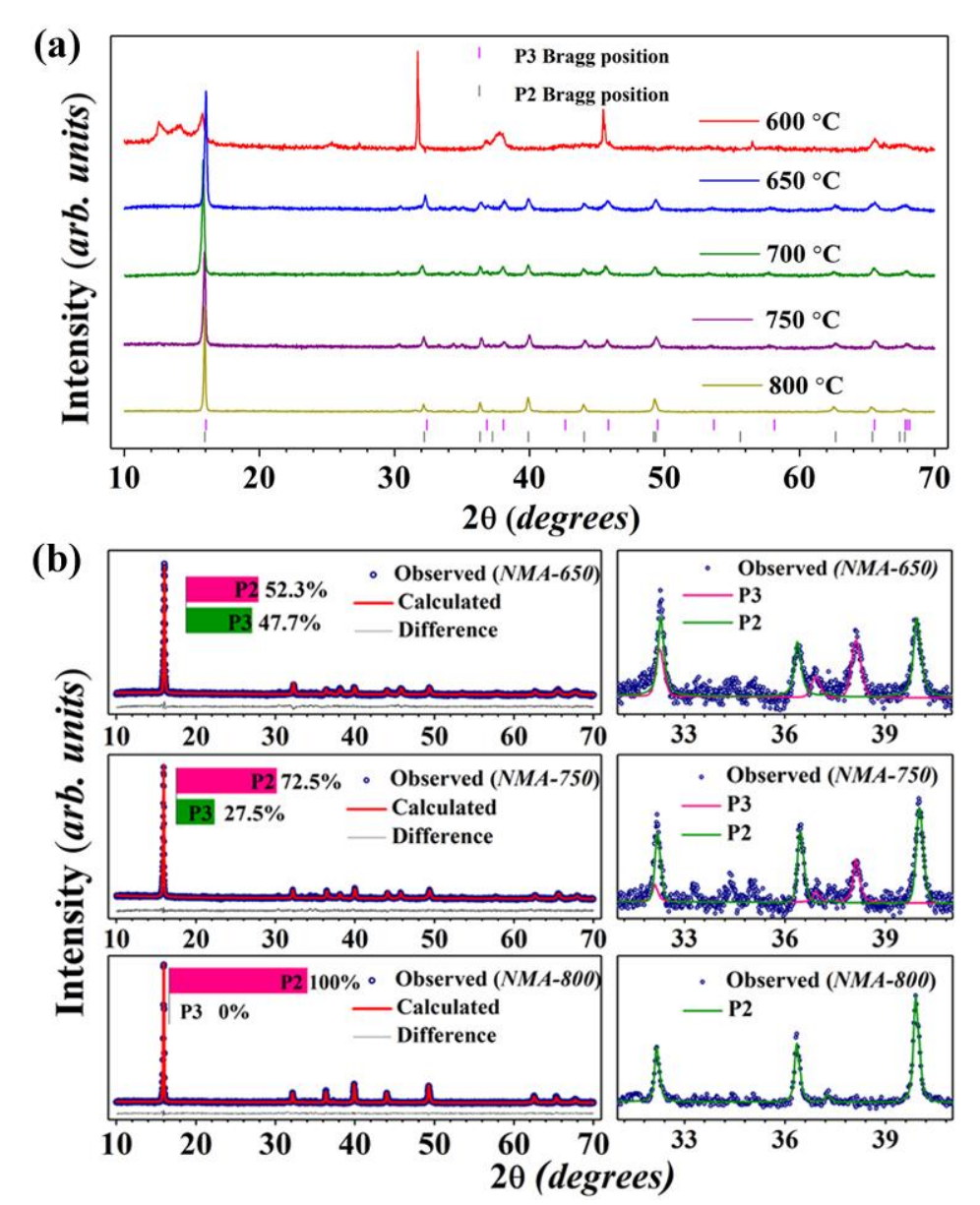


Fig. 1 (a) Phase evolution of Na_{0.75}Mn_{0.75}Al_{0.25}O₂ samples at various calcination temperatures along with brag positions of P3 (JCPDS: 04-020-1860) and P2 (JCPDS: 27-0751) type structures. (b) Rietveld refinement of room temperature XRD data belonging to NMA-650, 750, and 850 samples, along with the deconvoluted P2 and P3 phases in the 2θ range of 30-40°.

Table 1. Lattice parameters of NMA-x samples obtained after the Rietveld refinement of room temperature XRD data.

Sample	Phase (Fraction)	a (Å)	c (Å)	$V(Å^3)$	Reliability Factors
NIM 4 (50	P3 (47.7%)	2.8500 ± 0.0003	$16.678 \\ \pm 0.003$	$117.47 \\ \pm 0.03$	R_{exp} : 1.73 R_{wp} : 2.30
NMA-650 -	P2 (52.3%)	2.8580 ± 0.0003	11.126 ± 0.001	78.81 ± 0.02	R_p : 1.79 GOF: 1.33
NMA-750 —	P3 (27.5%)	2.8453 ± 0.0003	16.716 ± 0.003	117.41 ± 0.03	R _{exp} : 2.12 R _{wp} : 2.51
	P2 (72.5%)	2.8491 ± 0.0002	11.137 ± 0.001	78.81 ± 0.01	R _p : 1.98 GOF: 1.18
NMA-800	P2 (100%)	2.8577 ± 0.0009	11.1474 ± 0.0008	78.839 ± 0.008	R_{exp} : 1.97 R_{wp} : 2.34 R_{p} : 1.84 GOF: 1.18

Further, the crystallographic parameters obtained from Rietveld refinement were used to simulate the Na ion migration pathways and calculate the migration energy barrier in the P3 and P2 type structures of NMA using the bond-valence site energy (BVSE) calculation. The calculated migration energy for Na⁺ in P2 and P3 type NMA was 0.181 eV and 0.237 eV, respectively (Fig. S1(a & b). The reaction pathway diagram of P2 and P3 type structures generated using VESTA [44] is shown in Fig. S1(c & d). Besides the higher activation energy, another drawback of using P3-type cathodes in Na-ion batteries is related to the multiple structural transformations P3 undergoes during cycling. These transformations lead to a lower Na⁺ conductivity and degrade the cathode's electrochemical performance. In addition to enhancing the overall conduction in the material, the P2 phase in the biphasic cathodes is expected to stabilise the P3 phase and prevent unwanted phase transitions during the charge/discharge process [25, 26].

The SEM micrographs on NMA-650, 750, and 800 displayed in Fig. 2 depicts hexagonally shaped grains consistent with layered oxides. The elemental map of NMA-750 is portrayed in Fig. 2(b1-b4). In NMA-650, the particles portray particles with well-defined contours and facets with a relatively lower degree of agglomeration. In contrast, the microstructure in NMA-750 and 800 display a higher degree of agglomeration, with particles fusing to form lumps in NMA-800. Particle morphology is an important parameter that affects electrochemical properties such as the rate performance of cathodes. Ideally, nano-size particles with a low degree of agglomeration are preferred in cathodes as it increases the total surface area of each particle (in contact with the liquid electrolyte) compared to its volume. As liquid electrolytes have higher ionic conductivities than cathode materials, nano-sized particles could effectively reduce the Na⁺ conduction path through the crystalline material, enhancing Na⁺ extraction/insertion during cycling, especially at high charge/discharge rates [45, 46]. Hence, NMA-650 is expected to show a better rate performance than the other samples during electrochemical testing.

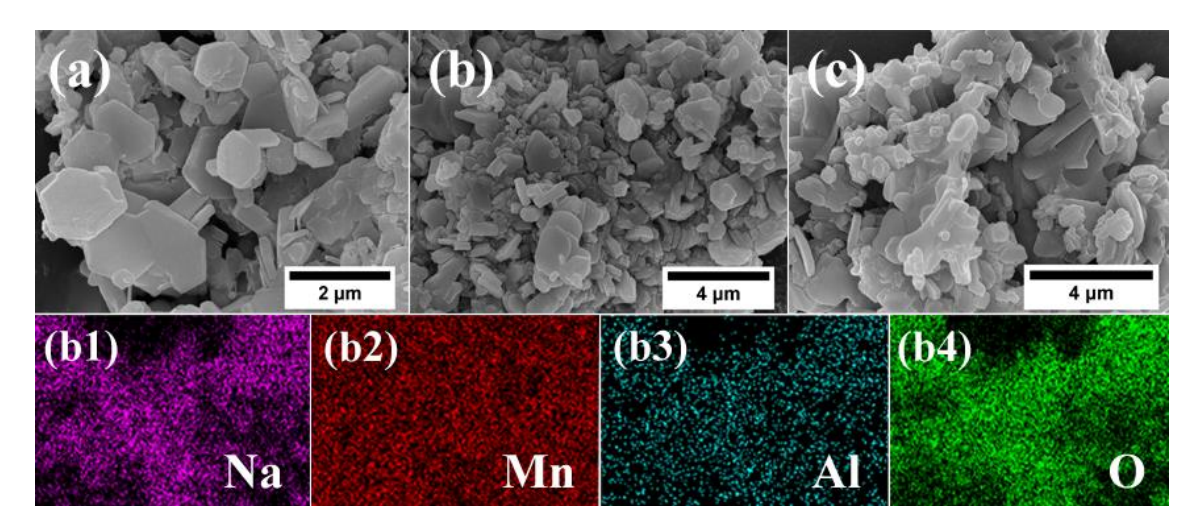


Fig. 2 SEM micrographs of (a) NMA-650, (b) 750, and (g) 800, along with (b1-4) elemental maps depicting the distribution of the Na, Mn, Al, and O in NMA-750.

The Mn 2p and Al 2s XPS spectra (Fig. 3) for NMA-650 and 800 samples were obtained to confirm the valence states of the Mn and Al ions in each compound. The peak at 85 eV in the

Al 2p spectra suggests the presence of Al³⁺ ions in all the samples [47-49]. In contrast, the Mn 2p XPS spectra can be deconvoluted into 4 peaks; the 2 coupled peaks at 641.8 & 653.2 eV belong to Mn³⁺, while those at 643.2 & 654.7 eV correspond to Mn⁴⁺ [22, 47, 48]. The similarity of Mn 2p XPS spectra of both samples indicates their similar Na⁺ contents. Lower Na⁺ content in either sample would alter the sample's peak intensity ratio of Mn³⁺ and Mn⁴⁺ ions. Hence, the P3 to P2 phase transformation observed in the NMA-*x* samples can only be driven by the better stability of P2 over the P3 at higher temperatures rather than due to the change in Na-ions concentration in the sample.

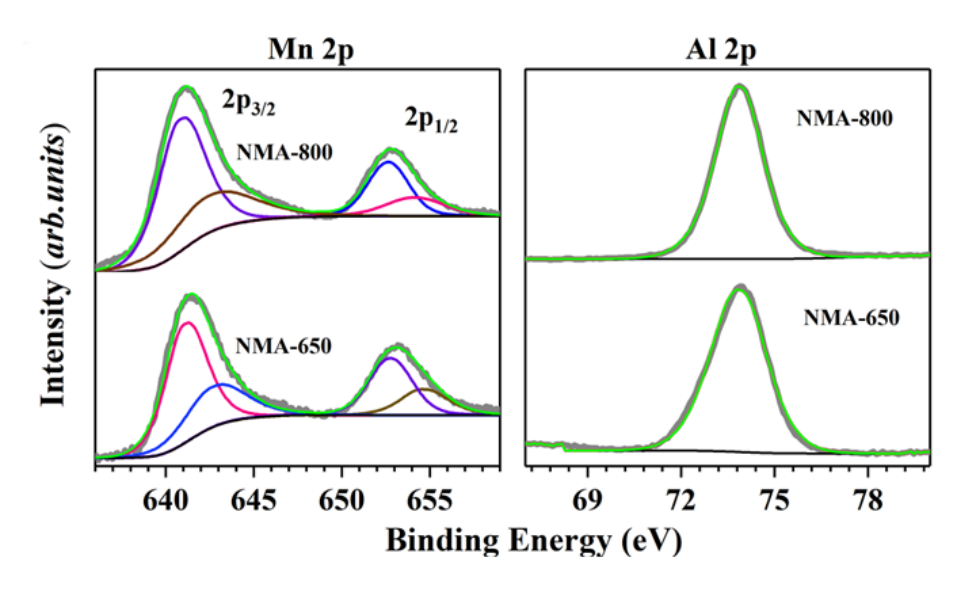


Fig. 3 XPS spectra of NMA-650 and NMA-800.

3.2 Electrochemical Characteristics

The electrochemical properties of the NMA-*x* cathodes were analysed between 1.5 V and 4.2 V using a coin cell with Na metal acting as the reference & counter electrode. The cyclic voltammograms in Fig. 4 show peaks indicating the redox activity of Mn ions below 3V in all the cathode materials [37, 50]. While the CV curves of NMA-650 show only a single redox peak, multiple peaks attributing the Mn^{3+/4+} redox reaction can be observed for NMA-750 and 800 samples. Multiple peaks attributed to the same redox reaction in the latter samples could indicate structural changes in the cathode materials caused by either Na-ion vacancy ordering

or Jahn-Teller active Mn^{3+} . Structural variations induced by the activity of Mn^{3+} are usually reported as the primary reason behind capacity fading in P2-type layered oxides where Mn is active [3, 21, 22, 50, 51]. In the P2 dominant NMA-750 and 800 samples, a higher amount of the P2 phase seems to be initiating a similar reduction in specific capacity with cycling as the peak intensities of the oxidation and reduction peak appear to be fading with each cycle along with the area under the curve. In contrast, the cyclic voltammogram of NMA-650 with $\sim 52\%$ P3 phase shows almost no reductions in peak intensities or area under the curves, suggesting better structural durability. As a result, a biphasic cathode could show better cyclic performance.

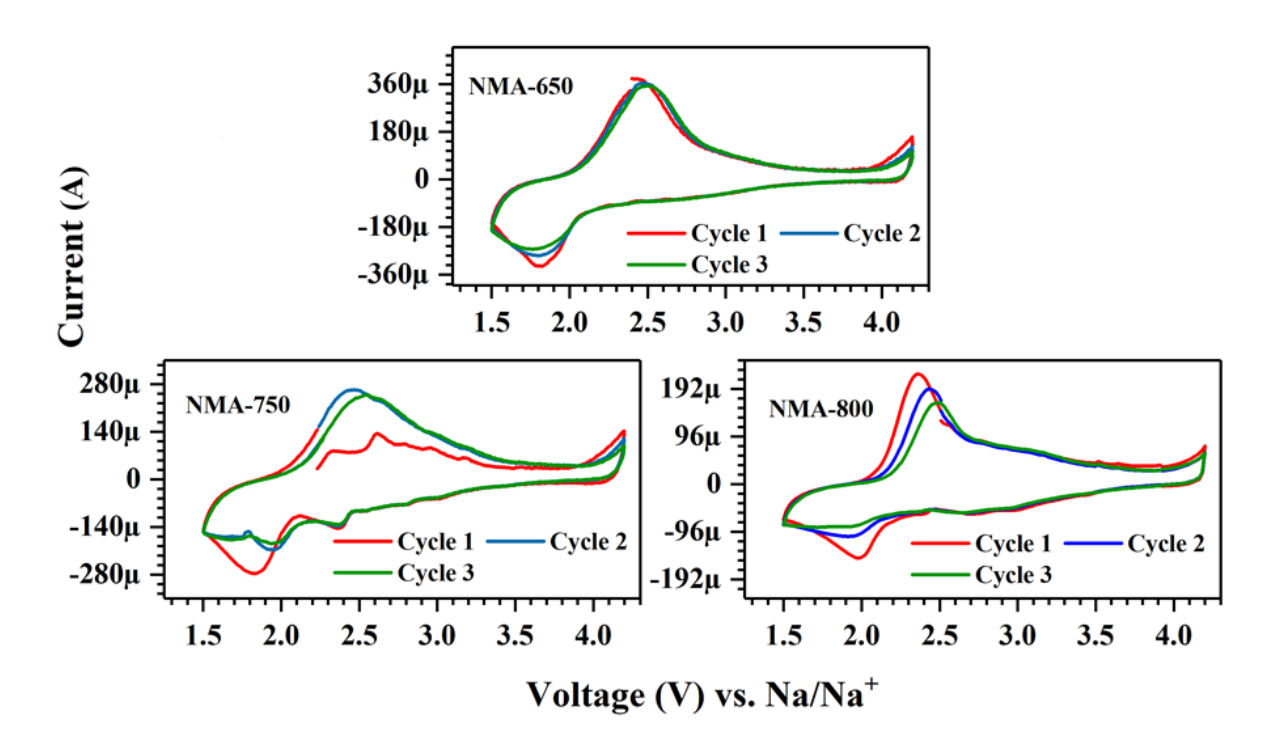


Fig. 4 Cyclic voltammograms of NMA-600, 750, and 800 samples.

The galvanostatic charge-discharge curves of NMA-650, 750, and 800, presented in Fig. 5, concur with the CV curves. The GCD curves show rapid voltage drops between 4.2 V and 3 V, with plateaus emerging only below 3V. This is also reflected in the dQ/dV vs. voltage curves (Fig. S2, Supplementary Information), as peaks (indicating the changes in slopes of

the GCD curve) between 1.5 V and 3 V. Overall, the NMA-650 exhibited the highest specific capacity, 150 mAh g⁻¹ at a discharge rate of 0.1C. With an increase in the P2 phase fraction, the specific capacity dropped to 139 mAh g⁻¹ in NMA-750 and 113 mAh g⁻¹ in NMA-800, which marks about a 32% decline in capacity from NMA-650. P3-type cathodes are generally reported to have higher specific capacities than P2-type materials, as these can accommodate more Na ions by undergoing a reversible transformation to O3-type structures) [19, 25, 26, 31]. Hence, a lower specific capacity in the cathodes with a dominant P2 phase is expected. In terms of the amount of Na⁺ extracted, 150 mAh g⁻¹ (in NMA-650) corresponds to about 0.55. while a specific capacity of 113 mAh g⁻¹ in NMA-800 corresponds to only about 0.40. Even with a higher Na⁺ extraction, the NMA-650 still exhibits a higher energy efficiency (Fig. S3) ~ 83%, compared to 76% for the monophasic NMA-800 cathode. This is an interesting observation, as in the NMA layered oxide cathodes, a higher specific capacity also means a higher concentration of Mn³⁺ at the end of the discharge cycle, which would induce higher stresses in the material that could trigger structural transformations that hinder energy efficiency. The higher capacity while maintaining an impressive energy efficiency points to the resilience of the NMA-650 biphasic cathode and could be attributed to the widely reported synergetic often found in multiphasic cathodes [25, 26, 30, 31].

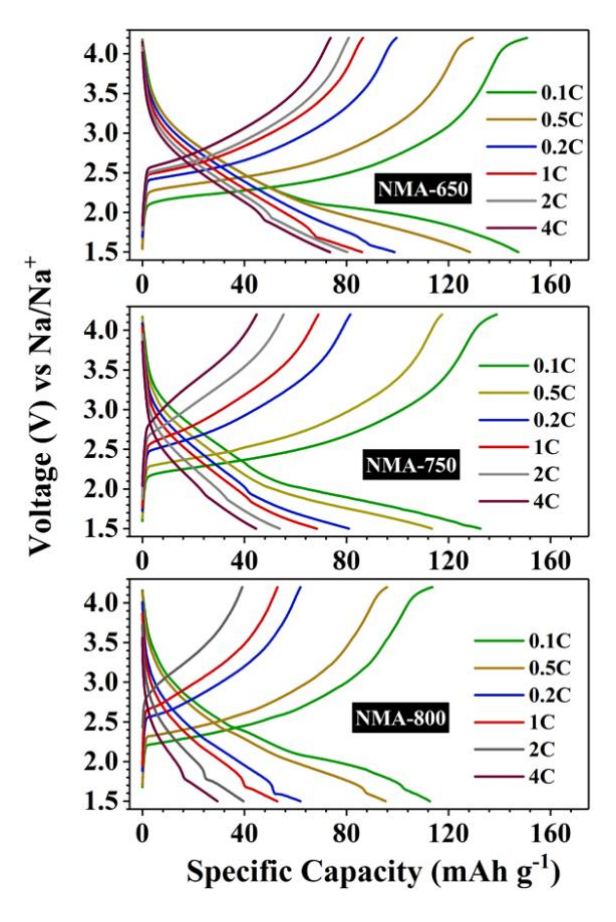


Fig. 5 GCD curves of NMA-x cathode materials at different C rates.

As the discharge rate increases from 0.1C to 4C, the specific capacities of all the cathodes deteriorate drastically (Fig. 5 and Fig. 6). NMA-650 shows a specific capacity of 80 mAh g⁻¹ and 73 mAh g⁻¹ at 1C and 4C, respectively. Even though 80 mAh g⁻¹ denotes a 42% reduction in capacity compared to the material's original capacity at 0.1C, it is still 30% higher than the P2-type cathode. While the presence of the P2 phase might have been beneficial in opening better Na⁺ conducting pathways within the material, the drastic reduction in specific capacity in NMA-650 suggests a decrease in diffusion coefficient with an increase in the C-rate. On the other hand, the unexpected drop in rate performance of the P2 dominant NMA-750 and 800 cathodes might be due to their agglomerated & fused particle morphologies that lowered the extraction of Na⁺ at high C rates by increasing the overall diffusion path for Na-ions in the cathode layer.

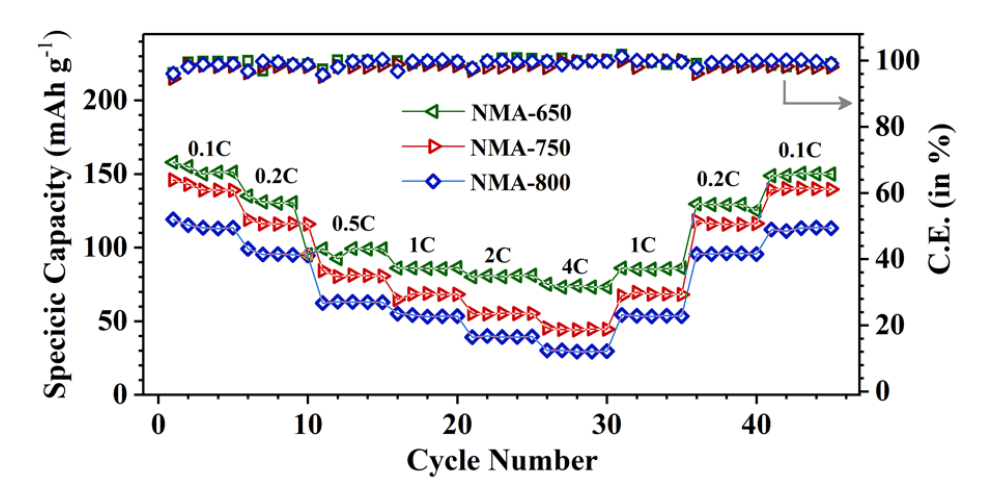


Fig. 6 Rate performance of NMA-x cathodes with C.E representing columbic efficiency.

Fig. 7 illustrates the cyclic performance of the cathodes at 1C when cycled between 1.5 V and 4.2 V. The data indicate that the specific capacity of the NMA-650 cathode dropped from 86 mAh $\rm g^{-1}$ to 67 mAh $\rm g^{-1}$, exhibiting an \sim 80% capacity retention after 200 cycles. In contrast, the other cathodes, NMA-750 and 800, showed a substantial reduction in specific capacity by being able to retain only about 67% and 56% of their original capacity at 1C.

Figure S4 shows the Nyquist plots of NMA-650 and 800 cells before and after 200 charge/discharge cycles. The figure shows a drastic increase in the total resistance of the NMA-800 cell (from 480 Ω to 970 Ω), while NMA-650 cell exhibits only a 50% increase in resistance after 200 charge/discharge cycles. Further, analysis of the Nyquist plot using equivalent circuit modeling revealed a 130% increase in charge transfer resistance in the cell with NMA-800 cathode. In comparison, the increase in resistance was \sim 60% in the cell with NMA-650 cathode (R1, R2, and R3 in the equivalent circuit in Fig. S4 inset denote the electrolyte resistance, SEI layer resistance, and charge transfer resistance, respectively [52-54]). The higher charge transfer resistance in NMA-800 could be due to structural degradation of the active material, side reactions, etc., causing the material to exhibit lower capacity retention than NMA-650 at the end of 200 charge-discharge cycles.

The excellent structural resilience of the NMA-650 cathode material predicted from the CV curves enabled it to harness the capacity obtained by activating Mn^{3+/4+} redox couple, which is usually avoided in Mn-based layered oxides due to its detrimental effects on cyclic performance. The improved cyclic stability of the NMA-650 over the other cathodes suggests that the adoption of a biphasic composition of the same material with nearly equal shares of P2 and P3 phases could be ideal for enhancing capacity retention in other layered oxide-based cathodes in literature where severe structural deformations have been identified as the primary cause of capacity degradation.

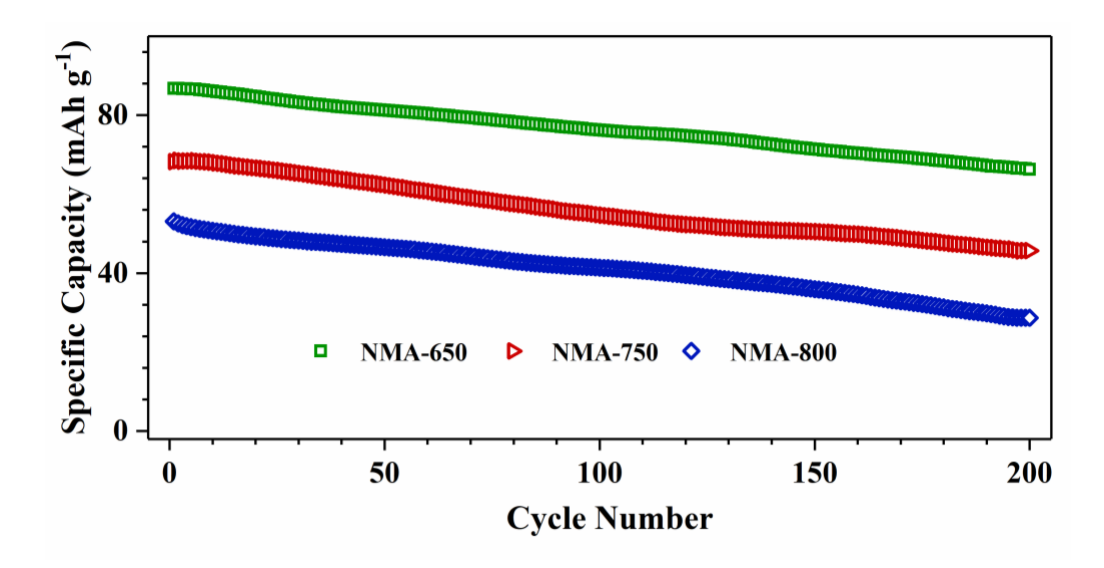


Fig. 7 Cyclic stability of NMA-x cathodes at a discharge rate of 1C.

Figure 8 shows the variation of Na⁺ diffusion coefficients in the NMA-x samples obtained from the galvanostatic intermittent titration technique (GITT). The technique, performed between a voltage range of 1.5 V – 4.2 V, involves the application of a constant current pulse for 10 minutes, followed by a dwell time of 30 minutes, during which the cell is allowed to reach a quasi-equilibrium state. This process is repeated till the cut-off voltages are reached. The diffusion kinematics of Na ion through the materials are assumed to obey Fick's first law, and the Na⁺ diffusion coefficient (D_{Na^+}) can be calculated using the following Eq. 1.

$$D_{Na^{+}} = \frac{4}{\pi \tau} \left(\frac{m_B V_m}{M_B S}\right)^2 \left(\frac{\Delta E_S}{\Delta E_{\tau}}\right)^2 \tag{1}$$

Here, M_B and V_m represent the molar mass and molar volume of the cathode material, m_B is the mass of active material, τ is the time of a single constant current pulse, and S denotes the active surface area of the electrode. ΔE_S and ΔE_{τ} represent the steady-state voltage change and voltage change during the constant current pulse, respectively. As expected, the diffusion coefficient of NMA-650 showed the highest diffusion coefficient of 2.5 $\times 10^{-10}$ while the diffusion coefficients of NMA-750 & 800 were $\sim 50\%$ lower. The lower diffusion coefficients at the onset of the charge/discharge process are due to a larger/smaller concentration of Naions within the structure, causing starvation of vacancies/ Na-ions.

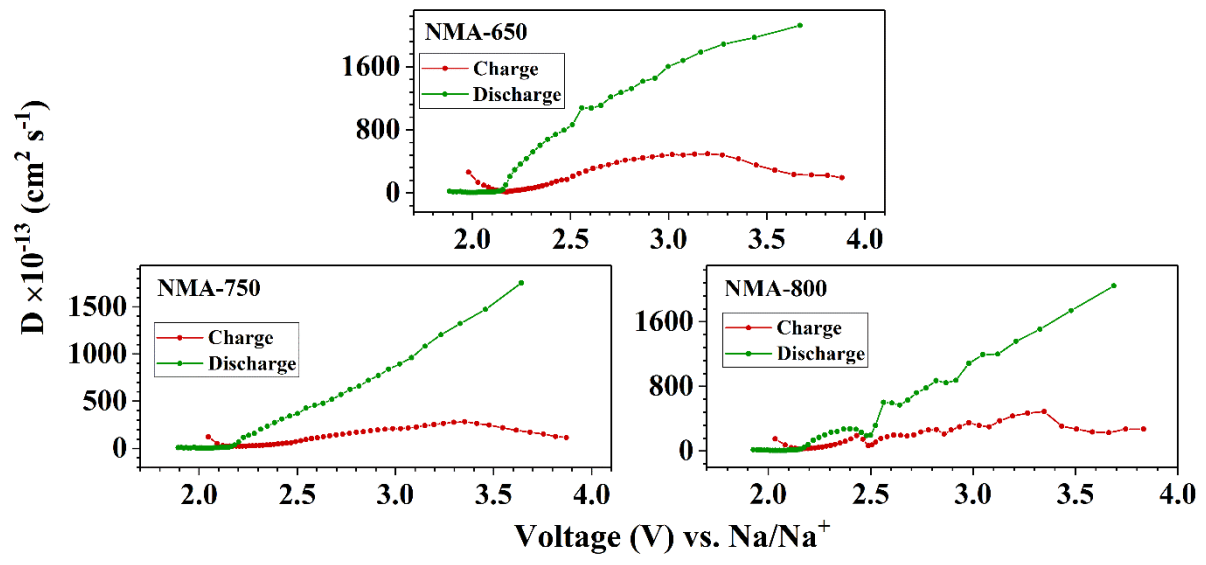


Fig. 8 Variation of diffusion coefficients of NMA-*x* cathodes during charging and discharging.

3.3 Operando Synchrotron XRD studies

The structural evolution of the material during the charge/discharge cycle could confirm many of the speculations regarding the electrochemical properties of NMA-*x* cathodes. Figure 9 and Fig. S6 illustrate the *operando* synchrotron XRD (SXRD) patterns NMA-650 and NNM-750 during the second cycle. The SXRD pattern of the NNM-650 sample obtained during the formation cycle (cycle 1) is displayed in Fig. S5. The data analysis for both the

cathode materials reveals an interesting detail, where a continued existence of the P3 phase is observed throughout the entire charge-discharge process. The P3 phase is usually reported to appear at higher voltages when the concentration of Na in the compound is below ~ 0.75 [19, 26, 29, 31]. At lower voltages, a P3→O3 phase transformation is expected. However, in both NMA-650 and 750, the P3-O3 phase conversion is not observed. The continued existence of the P3 phase also explains the improved cyclability and rate performance of the biphasic compounds, as the P3 phase is known to have a higher diffusion coefficient as compared to the O3 phase. The continued existence of P3 phase transformations in layered oxides is rarely reported and could result from a relatively high Al content in the compound. Even at a low voltage of 1.5 V, where Na concentration in the unit cell exceeds ~ 0.8 in NMA-650, the P3 structure appears stable across the voltage window. During the first discharge cycle, the P3 phase contracts along the c axis, where c reaches a value of ~ 16.59 Å at the end of discharge. In the subsequent charge-discharge cycle, the c axis expands to only about 16.66 Å at the fully charged state as opposed to its initial value of 16.69 Å at the pristine state, as evidenced by the presence of 2 peaks between 7-8° in Fig. 9 as opposed to a single broad & asymmetric peak at the start of the first charging cycle (Fig. S5).

Regarding volume expansion, the NMA-650 only shows an increase of only about 0.5%, which is marginal compared to the 1.5% in NMA-750, where c increased from 16.74 Å to 17.01 Å. The P2 phase shows almost no volume changes and behaves like a pillar within the material. During charging/discharging, the P2 layers remain almost invariant; hence, stress develops at the phase boundary in a direction opposite to the gliding direction of TMO2 layers in the adjacent P3 phase (normally, the gliding motion of the TM-O2 layers is initiated when the change in c parameter of the unit cell reaches a critical value and is responsible for the P3-O3 phase transitions), which restrains the transition metal layers from gliding. This

synergetic interaction between the two phases interlocks the TM-O₂ layers of adjacent P2 and P3 layers, which ensures better stability to the P3 structure [25, 26, 30, 31].

In both the compounds, most of the change in the c parameters occurs below 2 V during the discharge cycle (indicated by a more significant degree of shift in (003) peak towards higher angles in Fig. 9, which is consistent with the results from the electrochemical tests where the $Mn^{4+/3+}$ reduction peaks were obtained below 2 V.

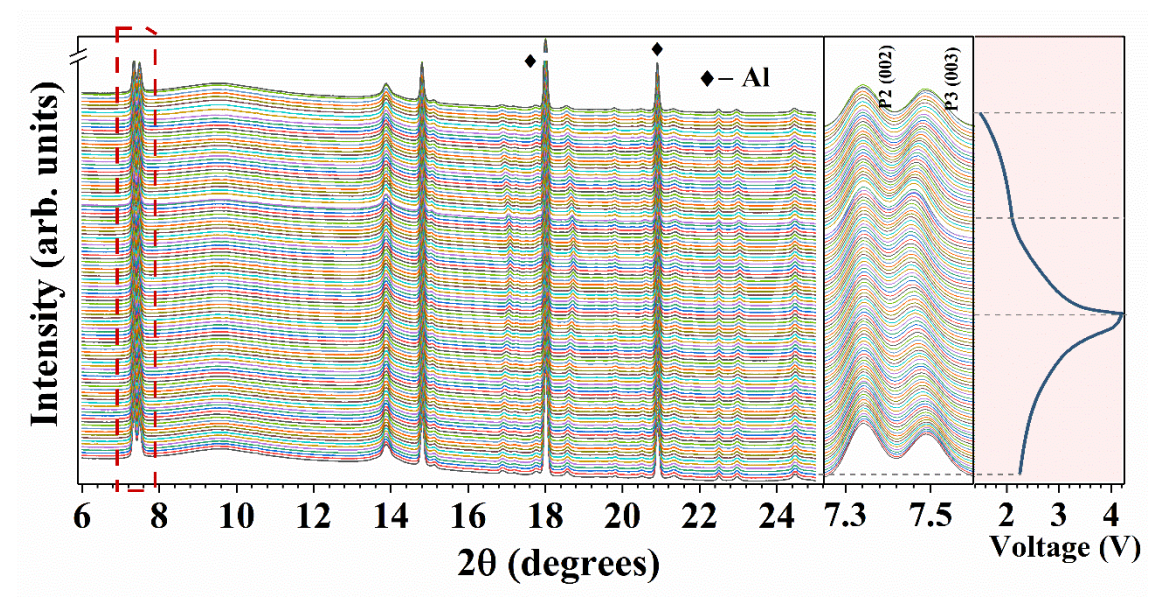


Fig. 9 *Operando* Synchrotron x-ray diffraction patterns of NMA-650 obtained during the second galvanostatic charge/discharge cycle at 0.1C.

4. Conclusions

P2/P3-Na_{0.75}Mn_{0.75}Al_{0.25}O₂ (NMA) compounds with varying P2 and P3 phase fractions were prepared via a sol-gel route. The phase fraction of the compounds was tuned by varying the calcination temperature. Rietveld refinement of XRD patterns confirmed the emergence of a P2/P3 phase material with ~ 52% P3 at 650 °C, with the amount of P3 reducing with increased calcination temperature. During electrochemical testing, the GCD curves of NMA-x samples showed a plateau below 2.5 V, which was reflected as a peak in their corresponding dQ/dV vs. voltage plots. The CV curves of NMA-650 showed overlapping oxidation and

reduction peaks after each cycle compared to diminishing peaks in other samples, allowing it to utilise the Mn^{3+/4+} redox process better. A high specific capacity of 150 mAh g⁻¹ (at 0.1 C between 1.5-4.2 V) with 80% capacity retained after 200 cycles at 1C (compared to 67% and 57% in NMA-750 and 800) is achieved by the NMA-650 sample. This sample also exhibited a better rate performance and a higher diffusion coefficient, attributed to its smaller particle size. *Operando* Synchrotron XRD studies of NMA-650 and 750 revealed the continuous existence of the P3 phase throughout the charge/discharge cycle, which is thought to be a consequence of a high Al content in the sample. In NMA-650, however, the change in the lattice parameter c of the P3 phase was significantly lower than in NMA-750, which may have been due to better interlocking due to the synergistic effect between the P2 and P3 phases.

Acknowledgements

SK is grateful for the financial support from the Science and Engineering Research Board (SERB), Government of India (grant number: CRG/2021/005548), and the Department of Science and Technology (DST), Government of India (grant no. DST/TMD/IC-MAP/2K20/01).

Declaration of Interest

The authors declare no conflict of interests.

References

[1] D. Buchholz, A. Moretti, R. Schmuch, S. Nowak, S. V, W. M, S. Passerini, Towards Naion batteries – Synthesis and Characterization of a novel high capacity Na-ion intercalation material, Chem. Inform, 160 (2013) 44 https://doi.org/10.1002/chin.201319014

- [2] J. Darga, J. Lamb, A. Manthiram, Industrialization of Layered Oxide Cathodes for Lithium-Ion and Sodium-Ion Batteries: A Comparative Perspective, Energy Technol., 8 (2020) 2000723 https://doi.org/10.1002/ente.202000723
- [3] R.J. Clément, P.G. Bruce, C.P. Grey, Review—Manganese-Based P2-Type Transition Metal Oxides as Sodium-Ion Battery Cathode Materials, J. Electrochem. Soc., 162 (2015) A2589-A2604 https://doi.org/10.1149/2.0201514jes
- [4] R. Usiskin, Y. Lu, J. Popovic, M. Law, P. Balaya, Y.-S. Hu, J. Maier, Fundamentals, status and promise of sodium-based batteries, Nature Rev. Mater., 6 (2021) 1020-1035 https://doi.org/10.1038/s41578-021-00324-w
- [5] L. Tan, Q. Wu, Z. Liu, Q. Chen, H. Yi, Z. Zhao, L. Song, S. Zhong, X. Wu, L. Li, Tisubstituted O3-type layered oxide cathode material with high-voltage stability for sodium-ion batteries, J. Colloid Interface Sci., 622 (2022) 1037-1044 https://doi.org/10.1016/j.jcis.2022.04.112
- [6] L. Qiao, X. Judez, T. Rojo, M. Armand, H. Zhang, Review—Polymer Electrolytes for Sodium Batteries, J. Electrochem. Soc., 167 (2020) 070534 https://doi.org/10.1149/1945-7111/ab7aa0
- [7] Mineral commodity summaries 2021, Mineral Commodity SummariesReston, VA, 2021, pp. 200.
- [8] C. Vaalma, D. Buchholz, M. Weil, S. Passerini, A cost and resource analysis of sodiumion batteries, Nature Rev. Mater., 3 (2018) 18013 https://doi.org/10.1038/natrevmats.2018.13
- [9] J. Peters, A. Cruz, M. Weil, Exploring the Economic Potential of Sodium-Ion Batteries, Batteries, 5 (2019) 10 https://doi.org/10.3390/batteries5010010
- [10] J.-Y. Hwang, S.-T. Myung, Y.-K. Sun, Sodium-ion batteries: present and future, Chem. Soc. Rev., 46 (2017) 3529-3614 https://doi.org/10.1039/C6CS00776G

- [11] X. Xiang, K. Zhang, J. Chen, Recent Advances and Prospects of Cathode Materials for Sodium-Ion Batteries, Adv. Mater., 27 (2015) 5343-5364 https://doi.org/10.1002/adma.201501527
- [12] C. Zhao, Z. Yao, Q. Wang, H. Li, J. Wang, M. Liu, S. Ganapathy, Y. Lu, J. Cabana, B. Li, X. Bai, A. Aspuru-Guzik, M. Wagemaker, L. Chen, Y.-S. Hu, Revealing High Na-Content P2-Type Layered Oxides as Advanced Sodium-Ion Cathodes, J. Am. Chem. Soc., 142 (2020) 5742-5750 10.1021/jacs.9b13572
- [13] H.N. Vasavan, M. Badole, S. Saxena, A.K. Das, S. Deswal, P. Kumar, S. Kumar, Excellent Structural Stability-Driven Cyclability in P2-Type Ti-Based Cathode for Na-Ion Batteries, ACS Appl. Energy Mater., 6 (2023) 2440-2447 https://doi.org/10.1021/acsaem.2c03750
- [14] S. Saxena, H.N. Vasavan, M. Badole, A.K. Das, S. Deswal, P. Kumar, S. Kumar, Tailored P2/O3 phase-dependent electrochemical behavior of Mn-based cathode for sodiumion batteries, J. Energy Storage, 64 (2023) 107242 https://doi.org/10.1016/j.est.2023.107242
 [15] C. Delmas, C. Fouassier, P. Hagenmuller, Structural classification and properties of the
- layered oxides, Physica B+C, 99 (1980) 81-85 https://doi.org/10.1016/0378-4363(80)90214-4
 [16] C. Ma, J. Alvarado, J. Xu, R.J. Clément, M. Kodur, W. Tong, C.P. Grey, Y.S. Meng, Exploring Oxygen Activity in the High Energy P2-Type Na0.78Ni0.23Mn0.69O2 Cathode Material for Na-Ion Batteries, J. Am. Chem. Soc., 139 (2017) 4835-4845 10.1021/jacs.7b00164
- [17] L. Zhang, J. Wang, J. Li, G. Schuck, M. Winter, G. Schumacher, J. Li, Preferential occupation of Na in P3-type layered cathode material for sodium ion batteries, Nano Energy, 70 (2020) 104535 https://doi.org/10.1016/j.nanoen.2020.104535

- [18] F. Wei, Q. Zhang, P. Zhang, W. Tian, K. Dai, L. Zhang, J. Mao, G. Shao, Review—Research Progress on Layered Transition Metal Oxide Cathode Materials for Sodium Ion Batteries, J. Electrochem. Soc., 168 (2021) 050524 https://doi.org/10.1149/1945-7111/abf9bf
 [19] X. Liang, T.-Y. Yu, H.-H. Ryu, Y.-K. Sun, Hierarchical O3/P2 heterostructured cathode materials for advanced sodium-ion batteries, Energy Storage Mater., 47 (2022) 515-525 https://doi.org/10.1016/j.ensm.2022.02.043
- [20] M. Li, D.L. Wood, Y. Bai, R. Essehli, M.R. Amin, C. Jafta, N. Muralidharan, J. Li, I. Belharouak, Eutectic Synthesis of the P2-Type NaxFe1/2Mn1/2O2 Cathode with Improved Cell Design for Sodium-Ion Batteries, ACS Appl. Mater. Interfaces, 12 (2020) 23951-23958 10.1021/acsami.0c04513
- [21] Z. Liu, X. Xu, S. Ji, L. Zeng, D. Zhang, J. Liu, Recent Progress of P2-Type Layered Transition-Metal Oxide Cathodes for Sodium-Ion Batteries, Chem. Eur. J., 26 (2020) 7747-7766 https://doi.org/10.1002/chem.201905131
- [22] W. Kang, D.Y.W. Yu, P.-K. Lee, Z. Zhang, H. Bian, W. Li, T.-W. Ng, W. Zhang, C.-S. Lee, P2-Type Na_xCu_{0.15}Ni_{0.20}Mn_{0.65}O₂ Cathodes with High Voltage for High-Power and Long-Life Sodium-Ion Batteries, ACS Appl. Mater. Interfaces, 8 (2016) 31661-31668 https://doi.org/10.1021/acsami.6b10841
- [23] L. Xian, M. Li, D. Qiu, C. Qiu, C. Yue, F. Wang, R. Yang, P3-type layered Na_{0.26}Co_{1-x}Mn_xO₂ cathode induced by Mn doping for high-performance sodium-ion batteries, J. Alloys Compd., 905 (2022) 163965 https://doi.org/10.1016/j.jallcom.2022.163965
- [24] H. Guo, M. Avdeev, K. Sun, X. Ma, H. Wang, Y. Hu, D. Chen, Pentanary transition-metals Na-ion layered oxide cathode with highly reversible O3-P3 phase transition, Chem. Eng. J., 412 (2021) https://doi.org/10.1016/j.cej.2021.128704

- [25] C. Hakim, H.D. Asfaw, R. Younesi, D. Brandell, K. Edström, I. Saadoune, Development of P2 or P2/P3 cathode materials for sodium-ion batteries by controlling the Ni and Mn contents in Na_{0.7}Co_xMn_yNi_zO₂ layered oxide, Electrochim. Acta, 438 (2023) 141540 https://doi.org/10.1016/j.electacta.2022.141540
- [26] Y.-N. Zhou, P.-F. Wang, Y.-B. Niu, Q. Li, X. Yu, Y.-X. Yin, S. Xu, Y.-G. Guo, A P2/P3 composite layered cathode for high-performance Na-ion full batteries, Nano Energy, 55 (2019) 143-150 https://doi.org/10.1016/j.nanoen.2018.10.072
- [27] J. Liu, C. Didier, M. Sale, N. Sharma, Z. Guo, V.K. Peterson, C.D. Ling, Elucidation of the high-voltage phase in the layered sodium ion battery cathode material P3–Na_{0.5}Ni_{0.25}Mn_{0.75}O₂, J. Mater. Chem. A, 8 (2020) 21151-21162 https://doi.org/10.1039/D0TA06600A
- [28] A. Tripathi, S. Xi, S.R. Gajjela, P. Balaya, Introducing Na-sufficient P3-Na_{0.9}Fe_{0.5}Mn_{0.5}O₂ as a cathode material for Na-ion batteries, Chem. Commun., 56 (2020) 10686-10689 https://doi.org/10.1039/D0CC03701J
- [29] T. Risthaus, L. Chen, J. Wang, J. Li, D. Zhou, L. Zhang, D. Ning, X. Cao, X. Zhang, G. Schumacher, M. Winter, E. Paillard, J. Li, P3 Na_{0.9}Ni_{0.5}Mn_{0.5}O₂ Cathode Material for Sodium Ion Batteries, Chem. Mater., 31 (2019) 5376-5383 https://doi.org/10.1021/acs.chemmater.8b03270
- [30] Y.-N. Zhou, Z. Xiao, D. Han, S. Wang, J. Chen, W. Tang, M. Yang, L. Shao, C. Shu, W. Hua, D. Zhou, Y. Wu, Inhibition of the P3–O3 phase transition via local symmetry tuning in P3-type layered cathodes for ultra-stable sodium storage, J. Mater. Chem. A, 11 (2023) 2618-2626 https://doi.org/10.1039/D2TA09277H
- [31] E. Lee, J. Lu, Y. Ren, X. Luo, X. Zhang, J. Wen, D. Miller, A. DeWahl, S. Hackney, B. Key, D. Kim, M.D. Slater, C.S. Johnson, Layered P2/O3 Intergrowth Cathode: Toward High

- Power Na-Ion Batteries, Adv. Energy Mater., 4 (2014) 1400458 https://doi.org/10.1002/aenm.201400458
- [32] Q. Pei, M. Lu, Z. Liu, D. Li, X. Rao, X. Liu, S. Zhong, Improving the Na_{0.67}Ni_{0.33}Mn_{0.67}O₂ Cathode Material for High-Voltage Cyclability via Ti/Cu Codoping for Sodium-Ion Batteries, ACS Appl. Energy Mater., 5 (2022) 1953-1962 https://doi.org/10.1021/acsaem.1c03466
- [33] Y. Chen, G. Su, X. Cheng, T. Du, Y. Han, W. Qiang, B. Huang, Electrochemical performances of P2-Na_{2/3}Ni_{1/3}Mn_{2/3}O₂ doped with Li and Mg for high cycle stability, J. Alloys Compd., 858 (2021) 157717 https://doi.org/10.1016/j.jallcom.2020.157717
- [34] Z. Lu, J.R. Dahn, In Situ X-Ray Diffraction Study of P2-Na_{2/3}[Ni_{1/3}Mn_{2/3}]O₂, J. Electrochem. Soc., 148 (2001) A1225 https://doi.org/10.1149/1.1407247
- [35] L. Yang, S.-h. Luo, Y. Wang, Y. Zhan, Q. Wang, Y. Zhang, X. Liu, W. Mu, F. Teng, Cudoped layered P2-type Na_{0.67}Ni_{0.33-x}Cu_xMn_{0.67}O₂ cathode electrode material with enhanced electrochemical performance for sodium-ion batteries, Chem. Eng. J., 404 (2020) 126578 https://doi.org/10.1016/j.cej.2020.126578
- [36] J. Xu, J. Chen, K. Zhang, N. Li, L. Tao, C.-P. Wong, Na_x(Cu–Fe–Mn)O₂ system as cathode materials for Na-ion batteries, Nano Energy, 78 (2020) 105142 https://doi.org/10.1016/j.nanoen.2020.105142
- [37] M.H. Han, E. Gonzalo, N. Sharma, J.M. López del Amo, M. Armand, M. Avdeev, J.J. Saiz Garitaonandia, T. Rojo, High-Performance P2-Phase Na_{2/3}Mn_{0.8}Fe_{0.1}Ti_{0.1}O₂ Cathode Material for Ambient-Temperature Sodium-Ion Batteries, Chem. Mater., 28 (2016) 106-116 https://doi.org/10.1021/acs.chemmater.5b03276

- [38] H.N. Vasavan, M. Badole, S. Dwivedi, S. Kumar, Structural and transport properties of P2-Type Na_{0.70}Ni_{0.20}Cu_{0.15}Mn_{0.65}O₂ layered oxide, Ceram. Int., 48 (2022) 28986-28993 https://doi.org/10.1016/j.ceramint.2022.04.206
- [39] P. Manikandan, D. Ramasubramonian, M.M. Shaijumon, Layered P2-type Na_{0.5}Ni_{0.25}Mn_{0.75}O₂ as a high performance cathode material for sodium-ion batteries, Electrochim. Acta, 206 (2016) 199-206 https://doi.org/10.1016/j.electacta.2016.04.138
- [40] H. Liu, X. Gao, J. Chen, J. Gao, S. Yin, S. Zhang, L. Yang, S. Fang, Y. Mei, X. Xiao, L. Chen, W. Deng, F. Li, G. Zou, H. Hou, X. Ji, Reversible OP4 phase in P2–Na_{2/3}Ni_{1/3}Mn_{2/3}O₂ sodium ion cathode, J. Power Sources, 508 (2021) 230324 https://doi.org/10.1016/j.jpowsour.2021.230324
- [41] J.W. Somerville, A. Sobkowiak, N. Tapia-Ruiz, J. Billaud, J.G. Lozano, R.A. House, L.C. Gallington, T. Ericsson, L. Häggström, M.R. Roberts, U. Maitra, P.G. Bruce, Nature of the "Z"-phase in layered Na-ion battery cathodes, Energy Environ. Sci., 12 (2019) 2223-2232 https://doi.org/10.1039/C8EE02991A
- [42] A. Coelho, TOPAS and TOPAS-Academic: an optimization program integrating computer algebra and crystallographic objects written in C++, J. Appl. Crystallogr., 51 (2018) 210-218 https://doi.org/10.1107/S1600576718000183
- [43] L.L. Wong, K.C. Phuah, R. Dai, H. Chen, W.S. Chew, S. Adams, Bond Valence Pathway Analyzer—An Automatic Rapid Screening Tool for Fast Ion Conductors within softBV, Chem. Mater., 33 (2021) 625-641 10.1021/acs.chemmater.0c03893
- [44] K. Momma, F. Izumi, VESTA 3 for three-dimensional visualization of crystal, volumetric and morphology data, J. Appl. Crystallogr., 44 (2011) 1272-1276 https://doi.org/10.1107/S0021889811038970

- [45] V. Pamidi, S. Trivedi, S. Behara, M. Fichtner, M.A. Reddy, Micron-sized single-crystal cathodes for sodium-ion batteries, iScience, 25 (2022) 104205 https://doi.org/10.1016/j.isci.2022.104205
- [46] Z. Zhang, R. Wang, J. Zeng, K. Shi, C. Zhu, X. Yan, Size Effects in Sodium Ion Batteries, Adv. Funct. Mater., 31 (2021) 2106047 https://doi.org/10.1002/adfm.202106047
- [47] J.F. Moulder, J. Chastain, Handbook of X-ray Photoelectron Spectroscopy: A Reference Book of Standard Spectra for Identification and Interpretation of XPS Data, Physical Electronics Division, Perkin-Elmer Corporation1992.
- [48] S. Hüfner, Photoelectron spectroscopy: principles and applications, Springer Science & Business Media2013.
- [49] W.-L. Pang, X.-H. Zhang, J.-Z. Guo, J.-Y. Li, X. Yan, B.-H. Hou, H.-Y. Guan, X.-L. Wu, P2-type Na_{2/3}Mn_{1-x}Al_xO₂ cathode material for sodium-ion batteries: Al-doped enhanced electrochemical properties and studies on the electrode kinetics, J. Power Sources, 356 (2017) 80-88 https://doi.org/10.1016/j.jpowsour.2017.04.076
- [50] L. Wang, Y.-G. Sun, L.-L. Hu, J.-Y. Piao, J. Guo, A. Manthiram, J. Ma, A.-M. Cao, Copper-substituted Na_{0.67}Ni_{0.3-x}Cu_xMn_{0.7}O₂ cathode materials for sodium-ion batteries with suppressed P2–O2 phase transition, J. Mater. Chem. A, 5 (2017) 8752-8761 https://doi.org/10.1039/C7TA00880E
- [51] L.A. Ma, R. Palm, E. Nocerino, O.K. Forslund, N. Matsubara, S. Cottrell, K. Yokoyama, A. Koda, J. Sugiyama, Y. Sassa, M. Månsson, R. Younesi, Na-ion mobility in P2-type Na_{0.5}Mg_xNi_{0.17-x}Mn_{0.83}O₂ ($0 \le x \le 0.07$) from electrochemical and muon spin relaxation studies, Phys. Chem. Chem. Phys., 23 (2021) 24478-24486 https://doi.org/10.1039/D1CP03115E

- [52] P. Vadhva, J. Hu, M.J. Johnson, R. Stocker, M. Braglia, D.J.L. Brett, A.J.E. Rettie, Electrochemical Impedance Spectroscopy for All-Solid-State Batteries: Theory, Methods and Future Outlook, ChemElectroChem, 8 (2021) 1930-1947 https://doi.org/10.1002/celc.202100108
- [53] A.C. Lazanas, M.I. Prodromidis, Electrochemical Impedance Spectroscopy—A Tutorial, ACS Measurement Science Au, 3 (2023) 162-193 https://doi.org/10.1021/acsmeasuresciau.2c00070
- [54] M. Li, X. Qiu, T. Wei, Z. Dai, Study of Predominant Dynamics on the O3-Type Layered Transition-Metal Oxide Cathode by Electrochemical Impedance Spectroscopy for Sodium-Ion Batteries, Langmuir, 39 (2023) 8865-8878 https://doi.org/10.1021/acs.langmuir.3c00931

[Supplementary Information]

Impact of P3/P2 Mixed Phase on the Structural and Electrochemical Performance of $Na_{0.75}Mn_{0.75}Al_{0.25}O_2$ Cathode

Hari Narayanan Vasavan ^a, Manish Badole ^a, Samriddhi Saxena ^a, Velaga Srihari ^b, Asish Kumar Das ^a, Pratiksha Gami ^a, Sonia Deswal ^c, Pradeep Kumar ^c, and Sunil Kumar ^{a,d,*}

^a Department of Metallurgical Engineering and Materials Science, Indian Institute of Technology Indore, Simrol, 453552, India.

^b High Pressure & Synchrotron Radiation Physics Division, Bhabha Atomic Research Centre, 400085 Mumbai, India

^c School of Physical Sciences, Indian Institute of Technology Mandi, Himachal Pradesh, 175005, India

^d Center for Electric Vehicle and Intelligent Transport Systems, Indian Institute of Technology Indore, Simrol, 453552, India.

* Corresponding Author, sunil@iiti.ac.in

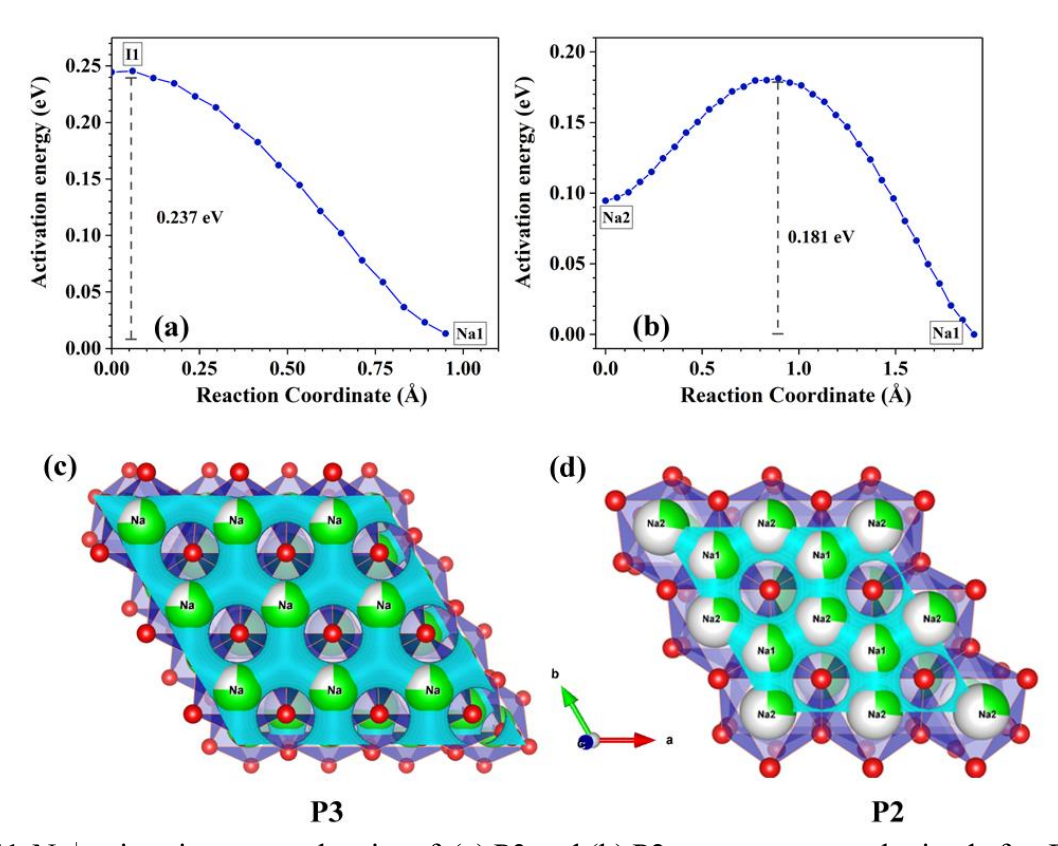


Fig. S1 Na⁺ migration energy barrier of (a) P3 and (b) P2 type structures obtained after BVSE analysis. Schematic of diffusion pathways (depicted in cyan) in (c) P3 and (d) P2 type structures. The I1 in (a) stands for interstitial site 1.

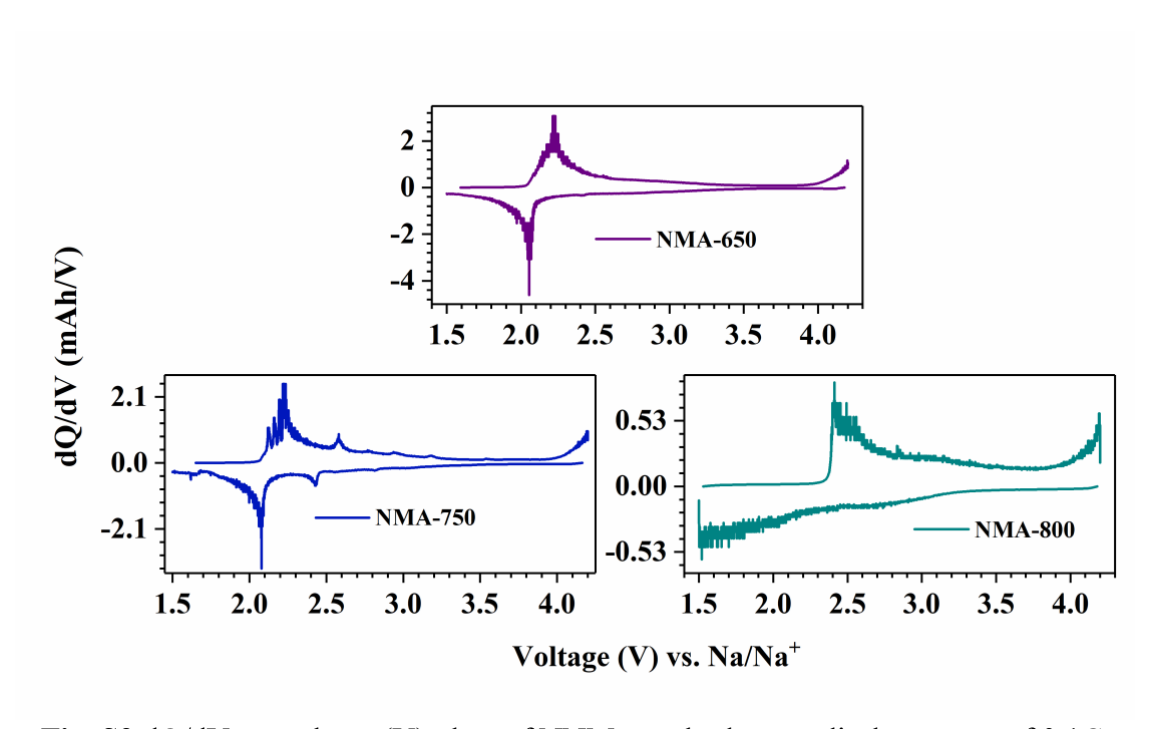


Fig. S2 dQ/dV vs. voltage (V) plots of NNM-x cathodes at a discharge rate of 0.1C.

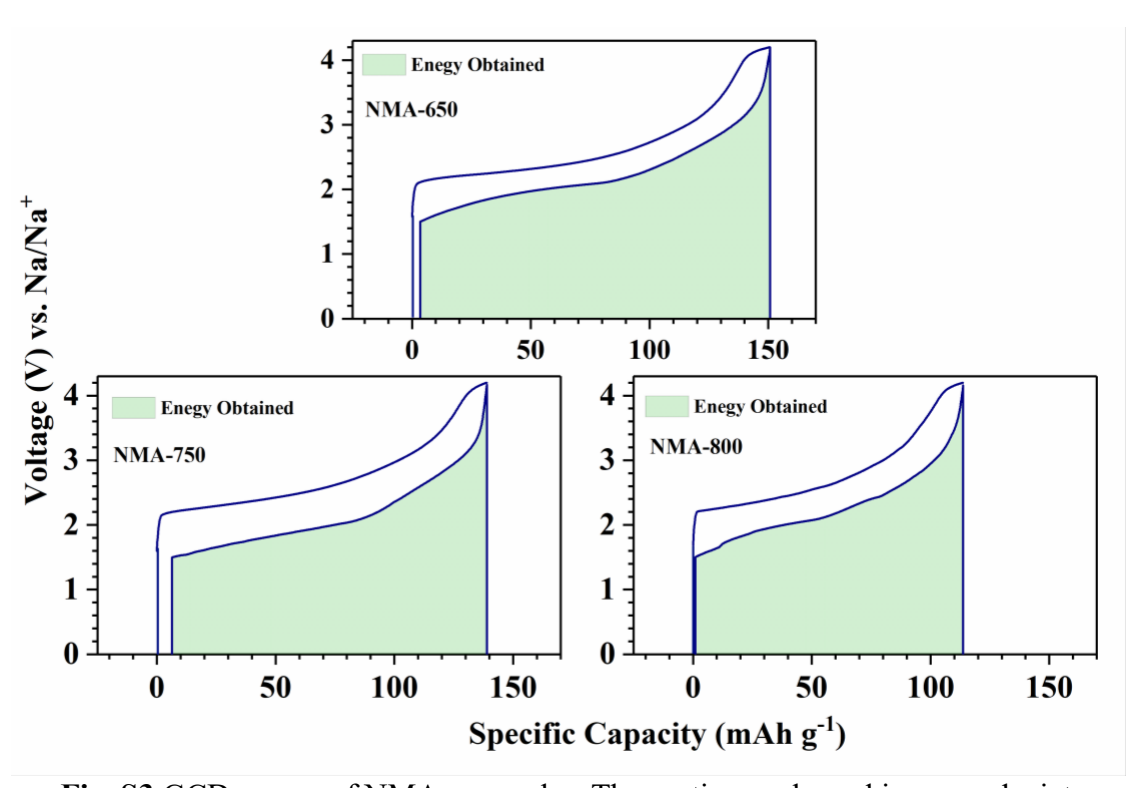


Fig. S3 GCD curves of NMA-*x* samples. The portions coloured in green depict energy recovered during discharge.

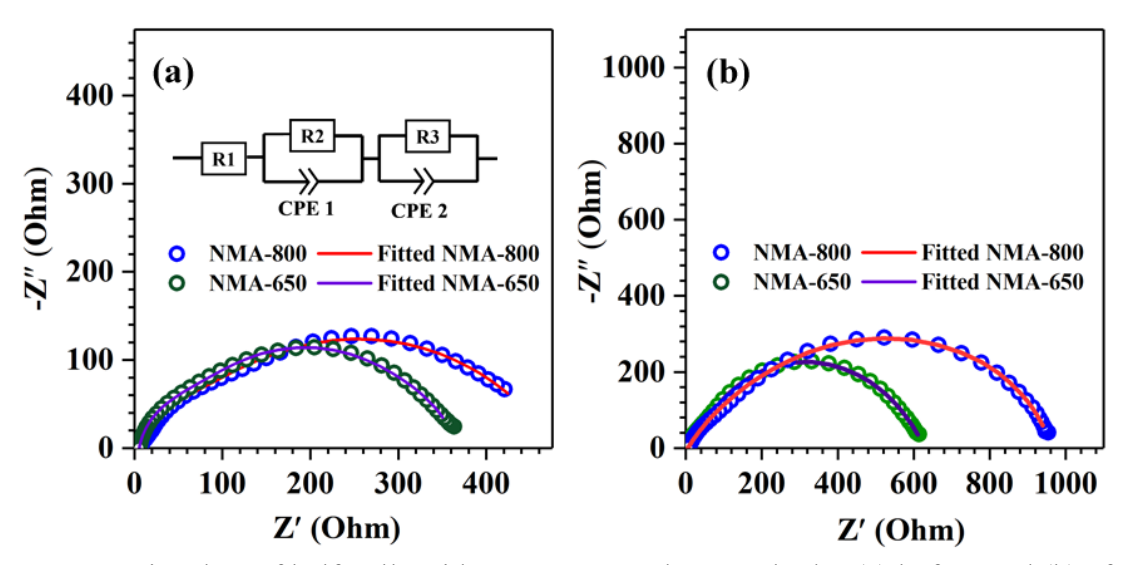


Fig. S4 Nyquist plots of half-cells with NMA-650 and 800 cathodes (a) before and (b) after cycling. The impedance data was fitted using the equivalent circuit shown in figure S4(a) inset.

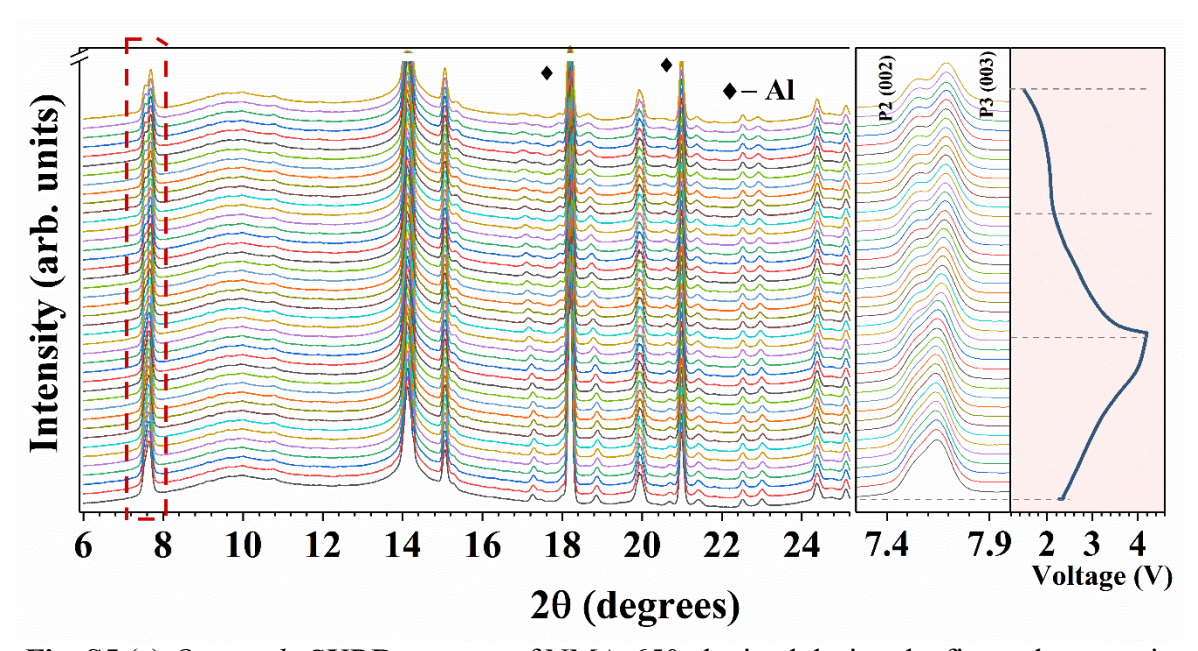


Fig. S5 (a) *Operando* SXRD patterns of NMA-650 obtained during the first galvanostatic charge/discharge cycle at 0.1C.

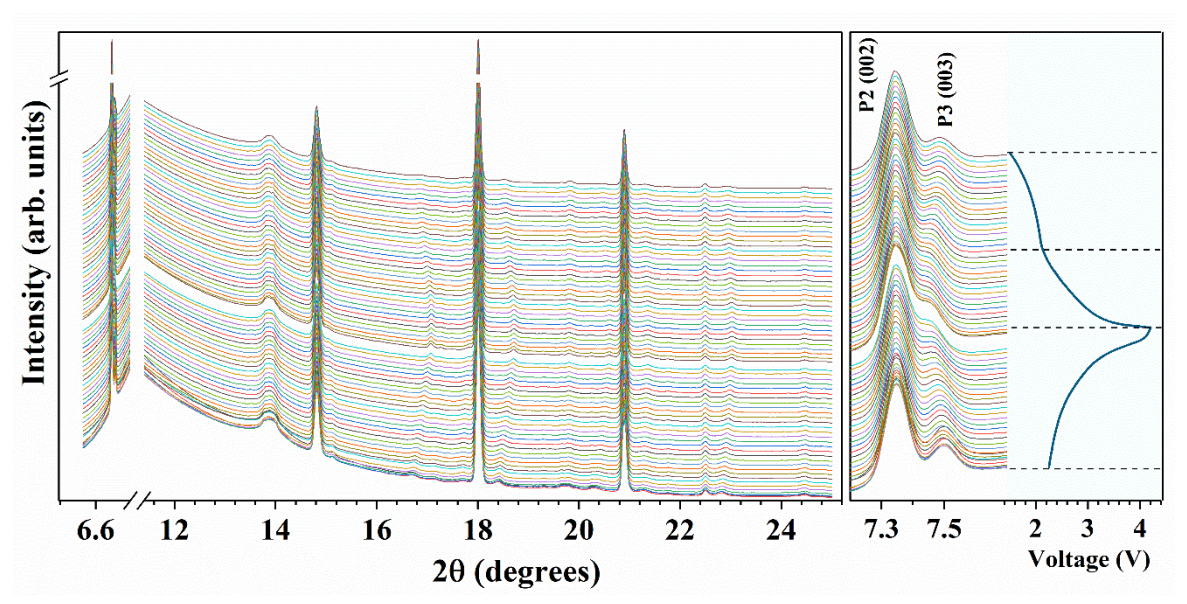


Fig. S6 (a) *Operando* SXRD patterns of NMA-750 obtained during the second charge/discharge cycle at 0.1C.

Table S1 Crystallographic parameters of P2-type NMA obtained from Rietveld refinement of room temperature XRD data.

P2 Type NMA (P63/mmc space group)							
Atom	Х	у	Z	Occupancy	Site		
Na1	2/3	1/3	1/4	0.45	2d		
Na2	0	0	1/4	0.30	2b		
Mn/Al	0	0	0	0.75/0.25	2a		
0	2/3	1/3	0.090	1	4f		

Table S2 Crystallographic parameters of P3-type NMA obtained from Rietveld refinement of room temperature XRD data.

	P3 Type NMA (R3m space group)								
Atom	X	у	Z	Occupancy	Site				
Na	0	0	0.17	0.75	3a				
Mn/Al	0	0	0	0.75/0.25	3a				
01	0	0	0.394	0.75/0.25	3a				
O2	0	0	0.607	1	3a				